DEM-FEM coupling method to simulate thermally induced stresses and local damage in composite materials

W. Leclerc, H. Haddad, M. Guessasma

Version of Record: https://www.sciencedirect.com/science/article/pii/S0020768318303998
Manuscript_23fb08aeb248b28dba9202c4a3fbf90b

DEM-FEM coupling method to simulate thermally induced stresses and local damage in composite materials

W. Leclerc[a], H. Haddad[b], M. Guessasma[a]

[a] *Université de Picardie Jules Verne, LTI, EA 3899, F-02100 Saint-Quentin, France*
[b] *European Ceramic Center, SPCTS, UMR CNRS 7315, F-87068 LIMOGES Cedex, France*

Abstract

The present contribution is dedicated to a coupling method mixing finite and discrete elements to simulate thermally induced stresses and local damage in composites. Investigations are focused on ceramic-metal materials which are characterized by a strong difference of properties and a coefficient of thermal expansion mismatch. Typically, thermal residual stresses are induced at the interface during a cooling process which can lead to dramatic effects on the local integrity of the joint. Some discrete approaches as the lattice beam model enable to simulate such effects but in somes cases lead to prohibitive calculation costs which affect their relevance. As a result, a coupling method taking benefit of both continuous and discrete approaches with a lower computational cost is of great interest. In this work, we investigate the DEM-FEM coupling approach based on a domain decomposition with overlapping area which has already proved its flexibility and its reliability in a large context. However, be aware that what is commonly called DEM-FEM coupling is in fact a beam lattice-FEM coupling approach in which the lattice network is generated using the contact network of a granular assem-

*corresponding author. Tel.: +33 323 503 697; fax: +33 323 503 698.
Email address: willy.leclerc@u-picardie.fr (W. Leclerc)

bly. Preliminary studies are first carried out to verify the ability of the coupling method to take into account the thermal expansion in homogeneous medium. In a second step, tests are performed in the framework of ceramic-metal fiber composites and compared to FE simulations in terms of stress and strain fields. Interfacial debonding effects are also studied. Finally, a classical ceramic-metal joint issue with local damage is simulated. In each case, results exhibit the relevance of the present approach to take into account thermal expansion and damage with a suitable accuracy. They also show a significant computation time decrease compared to FEM and DEM.
Keywords: DEM-FEM coupling method, Domain decomposition, Thermal expansion, Stress field, Damage

1. Introduction

Composite materials are more and more used in many industrial sectors and a large range of applications. Thus, fibre-reinforced composite materials characterized by an excellent stiffness-to-weight ratio are particularly popular in the field of high-performance products able to resist to hard conditions such as aerospace components, sport accessories, automobile engine devices, solar panel substrates or even surgical instruments. Sandwich materials are more specifically considered in airplane structures for thermal insulation and the dampening of vibration and noise, and woven ones have the benefit to be easily molded in complex shapes which make them good candidates for applications as, for example, a piece of propeller blades, auto bodies or drive shaft. However, independently of current enviromental and cost issues, joining two materials with different properties with a high integrity remains a real challenge. Thus, in the field of ceramic-metal ma-

terials, the reliability of the joint greatly depends on the nature of the interface bond and the Coefficient of Thermal Expansion (CTE) mismatch. In fact, thermal residual stresses are induced in the joint during the cooling process due to CTE mismatch and the difference of properties between metal and ceramics. These can dramatically reduce the joint strength and lead to local damage. Therefore, a great effort is required to propose new processes as well as numerical methods to better predict and control the potential implications of such interfacial issues in terms of integrity and lifecycle of composites.

In the last decades, numerous analytical and numerical tools have been developed to predict the multi-scale and multi-physics behavior of composite materials. Thus, Hashin-Shtrikman bounds [1], the Mori-Tanaka model [2] and other formulations based on probabilistic quantities [3] provide estimates of macroscopic properties such as mechanical and thermal ones as a function of a set of microstructural parameters. Numerical approaches such as the Finite Element Method (FEM) and the Fast Fourier Transform (FFT) based method [4] are often preferred when composites exhibit an intricated microstructure with a given level of entanglement. However, this class of materials is prone to several complex phenomena among others the local damage, the interfacial debonding and variability effects which are not easily taken in account in classical simulations. Similar to peridynamics [5], the Discrete Element Method (DEM) is more suited to characterize the multi-scale behavior of materials in which discontinuities and cracks arise under dynamic loadings. DEM was initially used in the field of rock mechanics [6] and later applied to a large scope of problems such as the wear mechanism [7], the subsurface damage from polishing [8], the silo discharge [9]

and the electromechanical modeling of ball bearing[10]. Cohesive bond models have also been developed to model continuous media and reproduce their mechanical [11, 12] and thermal [13, 14] properties using DEM, and applied to the context of heterogeneous media [15, 16]. Typically, cohesion is introduced at the scale of the elementary contact using a classical spring element but recent works [17, 18] take benefit of a cohesive beam model based on Euler-Bernoulli theory. This proved to be relevant to simulate the constitutive behavior of materials and model complex crack patterns with bifurcating and branching [19, 20, 21]. More recently, models have also been developed to consider the interfacial debonding [20, 21], non-linear effects [22] and the thermo-elastic coupling [23, 24, 25, 26]. However, in spite of new developments in terms of parallel implementation, such an approach remains poorly efficient when massive dynamic calculations are required. As a result, a great effort has been made in the last fifteen years to set up efficient coupling methods able to take into account very thin information at the microscopic scale with a lower computational cost [27, 28, 29]. The DEM-FEM coupling method used by Frangin et al. [27] and Rousseau et al. [30] is based on a domain decomposition with overlapping area and has the great advantage to be very flexible and benefit of a suitable background literature.

In the present contribution, we aim at investigating the ability of the DEM-FEM coupling method used by Frangin et al. [27] and Rousseau et al. [30] to simulate the thermal-induced damage in material composites. First of all, one must keep in mind that it enables to couple a continuous model to a granular system bonded by beam or spring elements and not directly to the DEM but the terminology "DEM-FEM" is nevertheless commonly used and will be preferred in what follows. Be-

sides, and for the same reason, the terminology "DEM" will refer to the cohesive beam based approach. This work is mainly motivated by the need to understand the limits and advantages of the coupling method in light of recent developments in DEM, especially those related to the simulation of thermo-mechanical behavior of composite materials and their damage. Typically, in a coupled discrete-continuous method, local areas where discontinuities and moderate cracks could occur are modeled using a set of Discrete Element (DE) and the homogeneous areas are modeled by Finite Elements (FE). Please notice that such a paradigm is not well-suited to model severe cracking since it requires large DE areas which dramatically affect the computational cost and prevent the method to fulfill its original efficiency purpose compared to full DE calculations. Discrete areas are modeled using the cohesive beam model which enables to simulate an effective medium [18] and its thermo-mechanical behavior [26] using a network of cohesive bonds described by Euler-Bernoulli beam elements. In this approach, a natural network of links is first extracted from a granular packing, then improved by a specific Delaunay triangulation process and replaced by a network of cohesive beam elements. A specific calibration process finally relates the effective mechanical properties to local coefficients associated to each cohesive bond. The thermo-elastic coupling is also introduced using a model of thermal expansion based on the dilatation of each beam element at the scale of the elementary contact [25, 26]. This enables to simulate local damage due to CTE mismatch using specific tools. Thus, cracks initiation and propagation are modeled by the Removed Discrete Element Failure (RDEF) criterion [31], and the interfacial debonding is modeled by the Discrete Damage Zone Model (DDZM) [32]. Figure 1 illustrates the main steps of the DEM-FEM coupling method to simulate the thermal-induced damage in

material composites. After the introduction, part 2 describes the cohesive beam model and different numerical tools enabling to simulate the thermo-elastic behavior of composite materials and their damage. Part 3 is dedicated to validation tests of the DEM-FEM coupling method in homogeneous medium without and with thermal expansion. The next part aims at investigating the ability of the coupling method to simulate the damage induced by CTE mismatch in the context of fiber-composites. The last part focuses on a application to a current issue in ceramic-metal joint.

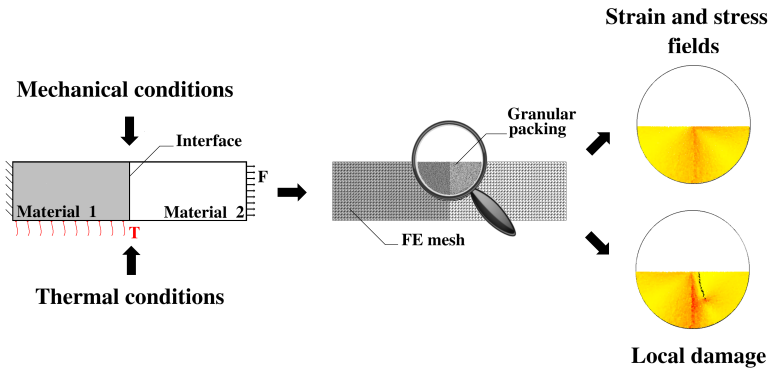

Figure 1: DEM-FEM coupling method to simulate the thermal-induced damage in material composites

2. Cohesive beam model

The present section describes the cohesive beam model based approach and several numerical tools introduced in previous works to simulate the thermo-mechanical behavior of materials. The basic idea is to reproduce a continuous medium using a granular packing composed of disks in contact. For that purpose, each contact is replaced by a cohesive beam element and the obtained lattice structure is associated to the discrete medium. Thus, we obtain a kind of hydrid model in which the

lattice structure enables to reproduce the effective behavior of the material and the discrete system gives the possibility to handle complex phenomena as damaging and contact.

2.1. Equivalent domain

The first step consists in generating an equivalent domain. Typically, we consider a granular system composed of disks in 2D or spheres in 3D which is generated under several assumptions of compacity, size, and arrangement of particles. In fact, previous works [17, 33] exhibited the great sensitivity of the macroscopic response to previous parameters. Besides, the representativity of our equivalent system strongly depends on the isotropy of the granular system which, to our knowledge, can only be ensured using random systems. That is why, our choice is to generate granular packings with the help of the efficient Lubachevsky-Stillinger Algorithm (LSA) [34] which enables an accurate control of the compacity and other parameters such as the size of particles and the coordination number. Thus, we can meet the assumptions of Random Close Packing (RCP) [35] the associated volumetric ratio of which is close to 85% for 2D systems. The suitable density of particles depends on the heterogeneity of the system and is a priori difficult to estimate. However, recent works [21, 26] showed that a minimum of about 5000 to 7000 particles is required to model a homogeneous square pattern independently of its dimensions. It corresponds to a criterion of about 70 to 80 particles along the side, which will serve as a basis for present studies. The isotropy of the granular system is closely related to particles arrangement which requires preliminary studies. Thus, a small size polydispersity is introduced in order to avoid undesirable directional effects. Typically, the particle's radius follows a Gaussian distribution law and the dispersion is described by a coefficient of variation set to

0.3 which remains small enough to not influence the results. A great care is also taken in the determination and the control of the coordination number Z which is the average number of particles in contact with a given one. This depends on a sensitivity parameter ε which enables to control the range of interaction between particles. We assume that bonds arise when the following relation is verified :

$$d_{ij} \leq R_i + R_j + \varepsilon \tag{1}$$

where d_{ij} is the center to center interparticle distance between two particles i and j in contact with radii R_i and R_j. Our choice is to adjust ε parameter in order to set Z to 4.5 which is a typical value for a 2D system. Finally, the randomness of contact angles between each pair of particles is verified using polar plots and the 2-point probability function as discussed in [36]. Please notice that, in the present work, the natural lattice structure of each granular system is densified using a specific Delaunay triangulation and its associated Voronoi tessellation [26]. Such a process turns out to be very practical since it avoids local flaws in the contact network and provides at the same time an area of representation to each DE and a transmission area to each contact. These two last parameters are specifically used in the thermo-mechanical coupling.

2.2. Elastic behavior

After generating the system, the second step of the present approach consists in introducing the cohesion at the scale of the elementary contact. Our choice is to use the beam element based on Euler-Bernoulli theory which yields a suitable effective medium as verified by several authors in the two last decades [11, 17].

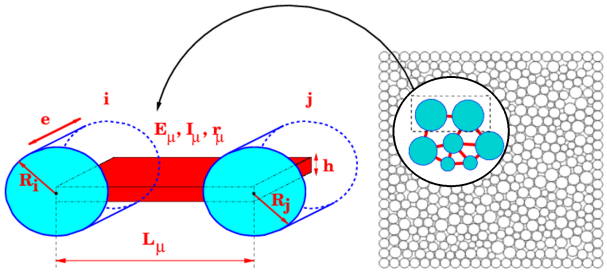

Figure 2: Cohesive beam model

2.2.1. Beam model

A cohesive beam element the formulation of which is given by Euler-Bernoulli model [18] is associated to each pair of particles in contact. This is characterized by a set of geometrical parameters, namely the length L_μ , the cross-section A_μ and the quadratic moment I_μ which are directly linked to the particles radii, and a local Young's modulus E_μ which is a priori not equal to effective Young's modulus of the system. For simplification purposes, we consider a quadrangular cross-section of height h which is defined as a function of particles size and reads :

$$h = r_\mu \frac{R_i + R_j}{2} \tag{2}$$

where R_i and R_j are respectively the radius of particles in contact i and j, and r_μ is a positive coefficient. Thus, all geometrical parameters only depend on r_μ and particles size. However, this latter is directly connected to the global density of particles which is generally chosen high enough to prevent any effect on the macroscopic behavior. From a mechanical standpoint, each cohesive link is controled by a vector of three-component generalized forces acting as internal forces

which are given by the following system :

$$\begin{bmatrix} \mathrm{F}_n^{j\to i} \\ \mathrm{F}_t^{j\to i} \\ \mathrm{M}^{j\to i} \end{bmatrix} = \begin{bmatrix} \mathrm{K}_n & 0 & 0 & 0 \\ 0 & \mathrm{K}_t & \frac{\mathrm{K}_t\mathrm{L}_\mu}{2} & \frac{\mathrm{K}_t\mathrm{L}_\mu}{2} \\ 0 & \frac{\mathrm{K}_t\mathrm{L}_\mu}{2} & \frac{\mathrm{K}_t\mathrm{L}_\mu^2}{3} & \frac{\mathrm{K}_t\mathrm{L}_\mu^2}{6} \end{bmatrix} \begin{bmatrix} \mathrm{u}_n^i - \mathrm{u}_n^j \\ \mathrm{u}_t^i - \mathrm{u}_t^j \\ \theta_i \\ \theta_j \end{bmatrix} \tag{3}$$

where superscripts n and t refer to the main directions of the local Cartesian coordinates system related to the contact between i and j particles. $\mathrm{u}_n^{i,j}$ and $\mathrm{u}_t^{i,j}$ are respectively the normal and tangential displacements associated to i and j particles. θ_i and θ_j are the components of rotation of particles i and j. K_n and K_t are the classical normal and tangential stiffnesses. Equations of motion for a given particle derive from internal cohesive forces and the numerical resolution is carried out by an explicit time integration which is well-adapted to compute large scale simulations and take into account complex phenomena with dynamics effects as damage or impact. A Rayleigh damping can also be added to internal forces in order to achieve a mechanical steady state. This point will be later discussed. DE calculations are performed over time which requires to define a suitable time step Δt. This is evaluated as function of critical time steps Δt_{crit}^c related to each cohesive beam element so that :

$$\Delta t \;=\; \frac{1}{\mathrm{k}} \min_{c\in\zeta}(\Delta t_{crit}^c) \tag{4}$$

where ζ is the set of contacts in the whole granular packing and k is a security coefficient chosen close to 2π according to [37].

2.2.2. Microscopic-macroscopic relation

We aim at correlating the macroscopic elastic response to sole microscopic coefficients E_μ and r_μ. To our knowledge, no correlation exists for the present co-

hesive beam model. That is why, macroscopic elastic properties E_M and ν_M are connected to local coefficients E_μ and r_μ using calibration curves obtained in our previous works [21, 26]. From a practical standpoint, a set of data is obtained for a large scale of configurations using specific quasi-static tests performed on square representative patterns composed of 7000 DE according to previous investigations [18, 21]. Results are treated to link local and global coefficients using polynomial regressions which directly provide the suitable pair of microscopic coefficients for an expected macroscopic response. Figures 3a and b illustrate the influence of r_μ

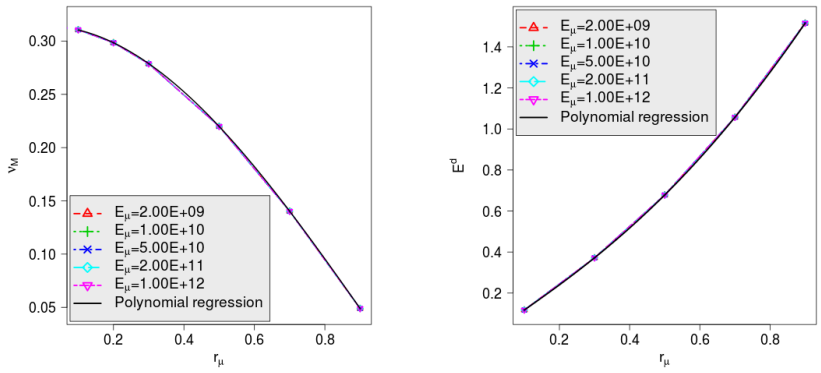

Figure 3: Microscopic-macroscopic relation (a) case of Poisson's ratio ν_M (b) case of dimensionless Young's modulus E^d

parameter on ν_M and the dimensionless Young's modulus E^d which is defined as the ratio between E_M and E_μ. For the present range of configurations, namely $E_\mu \in$[2GPa,1000GPa] and $r_\mu \in$[0.1,0.9], it is interesting to notice that E_μ has no impact on calibration curves so that the determination of the suitable pair of local parameters can simply be performed as follows. First, the user evaluates r_μ parameter using Figure 3a. Then, Figure 3b provides E^d as a function of this same parameter. Finally, E_μ is calculated from E^d and the expected macroscopic Young's modulus E_M. However, one has to know that the microscopic-macroscopic rela-

tion strongly depends on the characteristics of the granular packing, namely the coordination number Z, the volume fraction of particles ϕ and the range of interaction between particles ε [33]. As a result, our calibration curves are only valuable for the configuration described in subsection 2.1 with Z set to 4.5 and ϕ set to 0.85. Besides, all mechanical configurations can not always be handled using the cohesive beam model. In fact, Poisson's ratio ν_M is limited to 1/3 in the context of a lattice model based on Delaunay triangulation.

2.3. Model of thermal expansion

The thermo-elastic behavior of the material is described using a model of linear

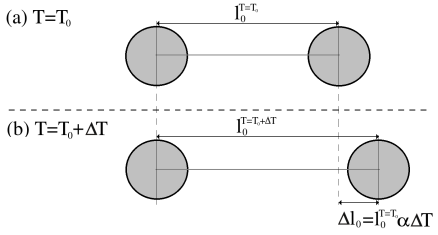

Figure 4: Thermal expansion of the beam (a) at T = T_0 (b) at T = T_0+ΔT

thermal expansion investigated by several authors [23, 24, 25]. In this approach, the whole domain is expanded without any additional forces or torques which means that under a homogeneous temperature field, thermal strains do not generate stresses for a relaxed homogeneous material . The model consists in modifying the free length $l_0^{T=T_0}$ of each beam element as a function of the temperature difference ΔT (Fig. 4) :

$$l_0^{T=T_0+\Delta T} = l_0^{T=T_0}(1 + \alpha\Delta T) \tag{5}$$

where α is the CTE associated to each beam element which is verified equal to the CTE of the effective medium [25, 26]. Please notice that an expansion of matter

is characterized by a positive ΔT, and a shrinkage by a negative ΔT. In the sequel, all temperature fields will be assumed homogeneous so that heat transfer is not considered in the present work. However, the interested reader could refer to one of our previous work on this subject [26].

2.4. Damaging

2.4.1. Stress and strain tensors

Generally, in DEM, cracks are modeled by breaking cohesive bonds using stress or strain criteria. However, it was proved that such models are irrelevant to simulate complex cracks pattern as the Hertzian cone in indentation test [21, 31]. As a result, we prefer to consider another approach based on the prediction of the Cauchy stress tensor at the scale of the particle using Zhou's formulation [38] :

$$\sigma_i \;=\; \frac{1}{2\Omega_i} \sum_{j \in Z_i} \mathrm{f}_{ij} \otimes \mathrm{r}_{ij} \tag{6}$$

where σ_i is the stress tensor associated to a given particle i. Prefix j designates a DE belonging to Z_i the set of particles linked to particle i. f_{ij} is the internal cohesion force vector applied to i by j and r_{ij} is the relative position vector between particles i and j. Ω_i is the area of representation provided by Voronoi tessellation. In the present contribution, the strain field is not used to predict cracks initiation and model their propagation. However, this provides interesting information to detect elastic areas induced by the mismatch of CTE in composite materials. The strain field is typically determined using a numerical tool called the fabric tensor [39] which is not easy to handle and requires additional calculations. In the present context, we prefer to consider the expression of the strain field proposed by Leclerc et al. [26] which takes benefit of a Voronoi tessellation to introduce

representative areas. Thus, ε_i the strain tensor associated to a particle i reads :

$$\varepsilon_i = \frac{1}{2\Omega_i} \sum_{j \in Z_i} A_{ij} n_{ij} \otimes \Delta_{ij} \tag{7}$$

where n_{ij} is the inter-particle normal vector, Δ_{ij} is the relative displacement between i and j particles and A_{ij} is the area of transmission between i and j particles which is given by the Voronoi mosaic.

2.4.2. Failure criterion

Crack propagation is modeled using the RDEF process introduced by André et al. [31]. The basic idea is to delete a particle when its equivalent stress tensor verifies a given failure criterion. Thus, in such an approach, mass conservation is not verified anymore when cracks initiate but the mass loss is limited to a low ratio of particles, typically less than 1% , for dense packings. The set of removed particles can then be seen as a set of ejected debris which do no interact anymore with the computational domain. In previous works [21, 25, 31], a hydrostatic stress based criterion was considered as failure criterion. However, even if such a criterion is suitable to model complex cracks pattern as the Hertzian Cone, this does not provide any information on the stress plane which does however play a key role in the brittle fracture mechanism. Besides we remind that, in the present contribution, we are only interested in failure of fragile materials such as alumina which have a strong ability to resist in compression and are consequently more sensitive to tensile solicitations. As a result, we prefer to consider the major main stress as criterion. Thus, the fracture is assumed to occur when σ_i^I the major main stress associated to a given particle i is greater than the Ultimate Tensile Strength (UTS) of the material :

$$\sigma_i^I > \text{UTS} \tag{8}$$

2.4.3. Interfacial debonding

In the context of 2-phase materials, the CTE difference between each phase can be a key factor leading to interfacial debonding according to thermal conditions (heating or cooling). In the present work, we consider an interfacial model derived from the Discrete Damage Zone Model (DDZM) introduced by Liu et al. [32] and discussed by Leclerc et al. in a previous contribution [21]. In this approach, cohesive beam elements connecting two particles belonging to two different phases are replaced by spring elements the normal stiffness of which K_n^Γ is defined as a function of the normal displacement u_n^Γ and the normal force F_n^Γ as follows :

$$F_n^\Gamma = K_n^\Gamma u_n^\Gamma \tag{9}$$

In a first linear regime, when $u_n^\Gamma < u_n^{\Gamma,c}$ where $u_n^{\Gamma,c}$ is a critical displacement, K_n^Γ is constant and equal to a given $K_n^{\Gamma,0}$ stiffness :

$$K_n^\Gamma \left(u_n^\Gamma < u_n^{\Gamma,c} \right) = K_n^{\Gamma,0} \tag{10}$$

In a second non-linear regime, when $u_n^\Gamma \geq u_n^{\Gamma,c}$, K_n^Γ explicitly depends on u_n^Γ and $u_n^{\Gamma,c}$ according to an exponential decrease so that K_n^Γ tends to zero for high displacements :

$$K_n^\Gamma \left(u_n^\Gamma \geq u_n^{\Gamma,c} \right) = \frac{1}{exp\left(\dfrac{u_n^\Gamma - u_n^{\Gamma,c}}{u_n^{\Gamma,c}} \right)} K_n^{\Gamma,0} \tag{11}$$

Thus, the normal stiffness K_n^Γ only depends on two parameters, namely the linear stiffness $K_n^{\Gamma,0}$ and the critical displacement $u_n^{\Gamma,c}$ which is a priori unknown. However, this is related to the interfacial stress limit σ_{lim}^Γ :

$$u_n^{\Gamma,c} = \frac{\sigma_{lim}^\Gamma A_\Gamma}{K_n^{\Gamma,0}} \tag{12}$$

where A_Γ is a cross-section associated to the spring element which is chosen equal to this of the corresponding cohesive beam element. From a practical standpoint, the microscopic stress limit $\sigma_{lim}^{\Gamma,c}$ related to a spring element has to be calibrated to match the expected macroscopic value σ_{lim}^{Γ}. For that purpose, several values of $\sigma_{lim}^{\Gamma,c}$ are preliminary tested until a good agreement is found between the observed result and σ_{lim}^{Γ}.

3. DEM-FEM coupling method

DEM can be seen as a potential alternative method to continuous approaches. In fact, this enables to more easily treat discontinuities and singularities than a classical method as FEM. Besides, this is also well-suited to take into account complex cracks pattern which occur at very fine scales. However, such an approach is poorly efficient in terms of computational cost which drastically affects its suitability to model complex materials which require massive calculations. As a result, different approaches have been proposed in the literature to couple discrete and continuous domains in order to take advantage of benefits proposed by a discrete approach without the calculation cost drawback [28, 29, 40, 41]. The present section focuses on a DEM-FEM coupling method as used by [27], [30] and [42]. This is based on the decomposition domain method with an overlapping sub-domain and weighting of energy.

3.1. Description

We consider a domain decomposition method based on a subdivision in three sub-domains : Ω_C is the continuous sub-domain discretized with FE, Ω_D is the discrete domain which is discretized with DE and Ω_O is an overlapping area composed of both FE and DE. Weighting coefficients are introduced inside the overlapping

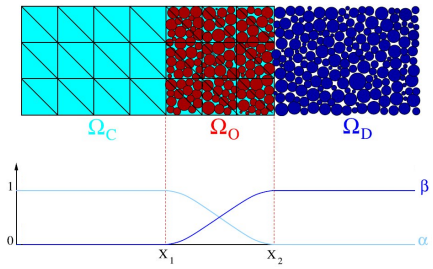

Figure 5: DEM-FEM coupling with overlapping domain, and definition of Ω_C, Ω_D and Ω_O sub-domains

sub-domain in order to avoid an overestimation of the mechanical energy. Thus, α and β respectively describe continuous and discrete ratio and vary from 0 to 1 inside the overlapping sub-domain and are constant elsewhere. Please notice that cubic polynomial functions are used to ensure a smooth transition inside Ω_O and $\alpha + \beta = 1$. Besides, from a practical standpoint, a small real ϵ is introduced to avoid singularities so that α and $\beta \in [\epsilon, 1 - \epsilon]$ with $\epsilon = 0.01$ [42].

We define the total energy H of the global domain as the weighted sum of energies associated to each sub-domain :

$$H(\mathbf{q}, \mathbf{u}) = \alpha H_c(\mathbf{q}) + \beta H_d(\mathbf{u}) \tag{13}$$

where H_c is the energy of the continuous sub-domain and H_d is the energy of the discrete sub-domain. $\mathbf{q}$ is the vector of continuous displacements and $\mathbf{u}$ is the vector of discrete displacements. The transition between $\mathbf{q}$ and $\mathbf{u}$ is ensured inside the overlapping sub-domain using the following kinematic continuity condition :

$$\mathbf{u} - D\mathbf{q} = 0 \tag{14}$$

where D is a coupling matrix which depends on the relative position of each DE within each FE and is only calculated one time. The kinematic continuity condi-

tion is taken into account using a vector of Lagrange multipliers $\boldsymbol{\lambda}$ the dimension of which is the number of DE inside the overlapping sub-domain :

$$L(\mathbf{q}, \mathbf{u}, \boldsymbol{\lambda}) = \alpha H_c(\mathbf{q}) + \beta H_d(\mathbf{u}) + \boldsymbol{\lambda}.(\mathbf{u} - D\mathbf{q}) \tag{15}$$

Thus, the final problem consists in minimizing the new functional L. One of the issues encountered when coupling FEM and lattice elements is related to wave reflection at the interface of discrete and continuous approaches. This well-known phenomenon is related to discretization difference between both methods. Typically, non-physical "ghost forces" occur and generate spurious reflected waves. Several authors have explored numerical methods to tackle such a drawback. Thus, Rousseau et al. [30] proposed some simplifications in the Lagrange method and Frangin et al. [27] introduced a relaxation parameter to reduce the values of Lagrange multipliers. More recently, Jebahi et al. [29] used a projection method in the context of a Constrained Natural Element Method (CNEM)-DEM coupling. Tu et al. [43] developed a generalized bridging domain method which takes benefit of independent weight functions and compensation forces. Besides, Chen et al. [44] proposed a novel DEM-FEM coupling approach using ghost particles, and Tu et al. [45] considered a multiscale separate edge coupling method to analyze the soil failure process. However, in spite of a great effort in the research community, the wave reflection issue is not completely solved at the present time. In this contribution, we only treat the wave reflection issue by filtering the smallest terms in the coupling matrix which leads to suitable results.

3.2. Validation tests

Validation tests are set up to exhibit the accuracy of the DEM-FEM coupling method and determine its ability to take into account thermal expansion. In a

first step, a numerical tensile test is performed using a 2D flat rectangular plate at ambient temperature which means that thermal effects are not taken account in this study. Then, in a second step, we investigate the case of a square domain only submitted to thermal solicitations during a cooling process.

3.2.1. Tensile test

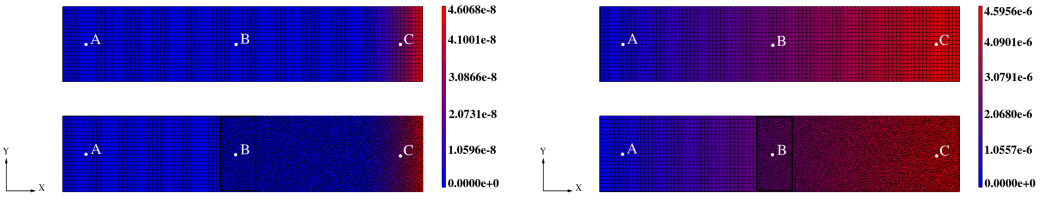

(a) t=5e^{-5}s (b) t=5e^{-4}s

Figure 6: Comparison of the displacement field between FEM and DEM-FEM coupling method

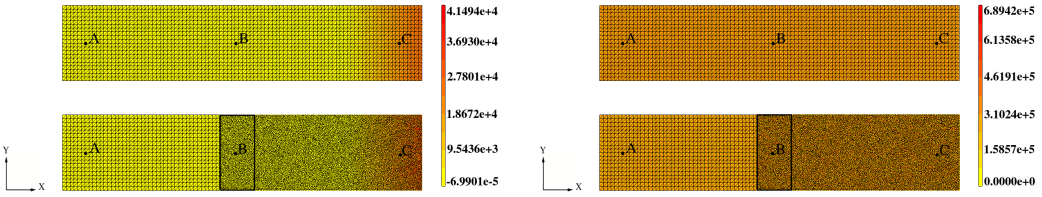

(a) t=5e^{-5}s (b) t=5e^{-4}s

Figure 7: Comparison of σ_{xx} field between FEM and DEM-FEM coupling method

	FEM			*DEM*			*DEM-FEM*		
	A pos.	B pos.	C pos.	A pos.	B pos.	C pos.	A pos.	B pos.	C pos.
u,t=5e^{-5}s	0	0	1.59e^{-8}	0	0	1.45e^{-8}	0	0	1.47e^{-8}
t=5e^{-4}s	4.24e^{-7}	2.30e^{-6}	4.23e^{-6}	4.08e^{-7}	2.30e^{-6}	4.20e^{-6}	4.21e^{-7}	2.28e^{-6}	4.19e^{-6}
σ_{xx},t=5e^{-5}s	0	0	1.27e^{4}	0	0	1.16e^{4}	0	0	1.16e^{4}
t=5e^{-4}s	2.25e^{5}	2.22e^{5}	2.21e^{5}	2.04e^{5}	2.52e^{5}	2.36e^{5}	2.24e^{5}	2.10e^{5}	2.45e^{5}

Table 1: Displacement (mm) and σ_{xx} (Pa) values at A, B and C positions

We consider a 2D flat rectangular plate of width l=0.23m, length L=1.104m and thickness e=0.01m. The domain is divided into two parts. The left part is located between x=0m and x=0.575m and discretized by a regular mesh composed of 2000 triangular FE. The right part is located between x=0.483m and x=1.104m and modeled by a granular packing composed of 14060 DE. The overlapping subdomain is located between x=0.483m and x=0.575m and composed of 2087 DE and 320 FE. Please notice that the number of particles is chosen so as to ensure a density of about 70 particles in the width which corresponds to about 5000 DE by square domain of side the width of the rectangular plate. The number of triangular elements is obtained under the assumption of one FE for 6 particles which leads to suitable results according to Haddad et al. [42]. The macroscopic Young's modulus E_M is set to 53.3 GPa and the Poisson's ratio ν_M is set to 0.157. These values correspond to E_μ= 56 GPa and r_μ=0.65 in the DE part. The density of the continuous model ρ_M is 2600 kg/m^3 and this of the discrete part ρ_μ is set to 3059 kg/m^3 in order to offset the porosity of the granular packing and ensure the mass equilibrium. A numerical tensile test is set up using the following configuration. The left edge is clamped and a time-dependent loading is applied to right one. The strength linearly increases from 0 to 500 N between t=0s and t=5e^{-4}s, and is set to 500 N for t>5e^{-4}s. Besides, no thermal effect is taken into account and no damping is considered. The time step is 1e^{-7}s and the total duration is 3.5e^{-3}s which corresponds to a total of 35000 time steps.

Figures 6a and b show the displacement field obtained using FEM and DEM-FEM coupling method at (a) t=5e^{-5}s and (b) t=5e^{-4}s respectively. For information purposes, FE comparisons are obtained using the same configuration than the

coupling method except for the mesh which is composed of 3840 triangular elements. From a qualitative standpoint, both displacement fields are very similar and the transition area exhibits no discontinuity. Numerical results are extracted from **A**(0.1m;0.115m), **B**(0.529m;0.115m) and **C**(1.004m;0.115m) positions and compared to full DE calculations performed in the same context using a granular packing composed of 25000 particles. These quantitative comparisons are given in Table 1. Results remain in good agreement whatever the method and the position with relative differences always less than 9% with respect to FE calculations. Figures 7a and b illustrate σ_{xx} stress field obtained using FEM and DEM-FEM coupling method at (a) t=5e^{-5}s and (b) t=5e^{-4}s respectively. Please notice that the stress tensor from which is derived σ_{xx} in the DE part is obtained using Zhou's formulation [38] as discussed in subsection 2.4.1. As previously seen for the displacement, stress fields are very similar without any discontinuity or singularity in the overlapping sub-domain. From a quantitative standpoint, stress values extracted from **A**, **B** and **C** positions show a good agreement between each method with a relative difference equal to 13% with respect to FE result in the worst case. Some comparison results of FEM, DEM and DEM-FEM coupling simulations are given in Figures 8a, b, c in terms of displacement, reaction strength, kinetic energy and potential energy. The displacement is obtained by averaging the contributions of each particle or node located to the right side of the plate. The reaction strength is determined by summing the contributions of the left side and energies are determined taking into account weighting parameters discussed in subsection 3.1. One can notice that, except for specific results obtained for a smaller overlapping area, all results are in good agreement with very low relative differences less than 3% whatever the method. In the case of the reaction strength, numerical outputs are

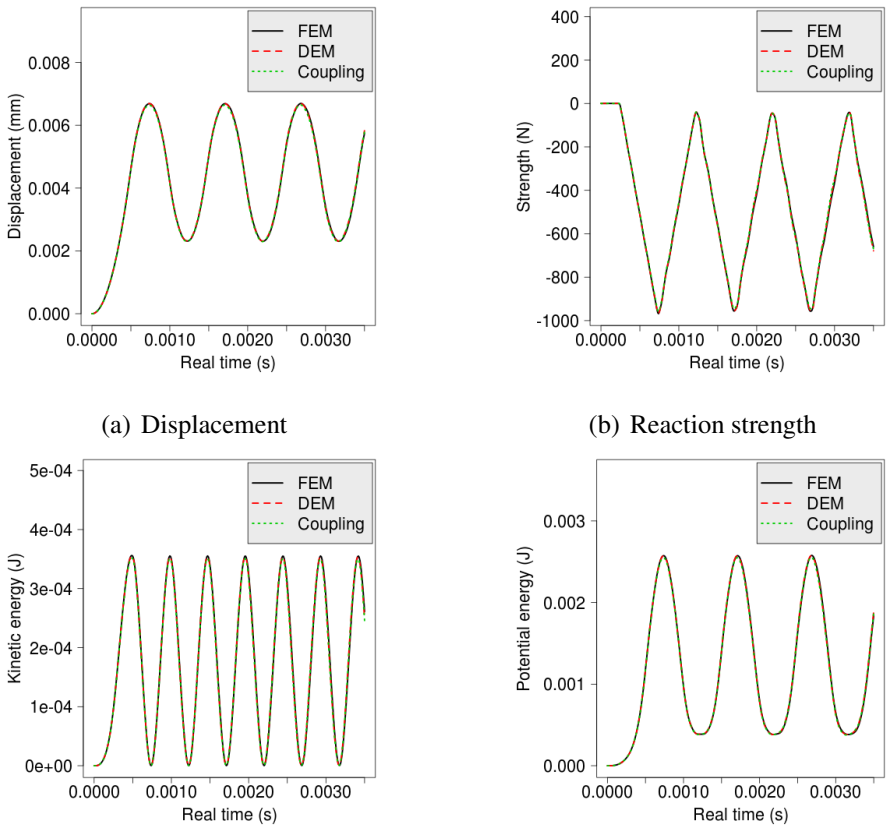

(a) Displacement

(b) Reaction strength

(c) Kinetic energy

(d) Potential energy

Figure 8: Comparison of FEM, DEM and DEM-FEM coupling simulations

obtained for several dimensions of the overlapping area according to l_c parameter which describes the ratio, expressed in percentage, of the width of the transition part to the total width of the plate. Three values are considered in our investigations. $l_c = 8.3\%$ corresponds to the reference case for which the width of the overlapping sub-domain is 0.092m. $l_c = 3.1\%$ and $l_c = 13.5\%$ lead respectively to a smaller and a larger transition area compared to the reference configuration. This study exhibits that larger the overlapping area is, more accurate results are. However, the intermediate value $l_c = 8.3\%$ turns out to be a good compromise between

accuracy and efficiency since a too large transition sub-domain leads to prohibitive calculation costs due to additional elements and particles. To conclude, the scope of present results highlights the suitability of the present DEM-FEM coupling approach to model an elastic medium under a dynamic loading. However, one has to keep in mind that precautions must be taken in the dimensions of the overlapping area to ensure the accuracy of numerical results.

3.2.2. Thermal expansion problem

The present test is dedicated to the study of the thermal expansion of a homo-

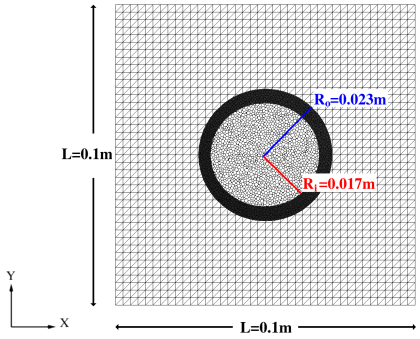

Figure 9: Definition of sub-domains in the DEM-FEM coupling method (case of thermal expansion problem)

geneous medium under a time-dependent homogeneous temperature field. We focus our investigations on a metallic material represented by a 2D square domain of side L=0.1 and thickness e=0.01m. As previously seen, the global domain is divided into three sub-domains. The continuous one corresponds to the square domain to which a centered disk of radius R_i=0.017m is removed. The discrete part is a centered disk of radius R_o=0.023m and the overlapping area is located between each centered disk of radii R_o and R_i respectively. For simplicity and efficiency purposes, the continuous part is discretized using a regular mesh composed

of 2892 triangular elements which does not strictly fit the circular boundary of the sub-domain but this has a priori no impact on our calculations as long as the mass equilibrium is verified. The discrete part is modeled by a granular packing composed of 2500 DE in order to ensure a ratio of about one FE for 5 particles. Thus, the overlapping area is finally composed of 1043 DE and 208 FE. We consider a homogeneous material composed of aluminum alloy of macroscopic Young's modulus E_M=69.1 GPa, Poisson's ratio ν_M=0.277 and CTE α=2.25e^{-5}K^{-1}. These values correspond to E_μ= 186.5 GPa, r_μ=0.3 and the same CTE in the DE part. Mass densities of continuous and discrete models are respectively ρ_M=2600 kg/m^3 and ρ_μ=3059 kg/m^3 in order to offset the porosity of the granular packing. Numerical computations are performed according to the following configuration. Symmetric boundary conditions are imposed at left and bottom edges of the square domain to enable the free expansion of the material. The temperature is varied over time so that the difference between initial and final temperatures T_0 and T is $\Delta T=T-T_0$=-10K and leads to a shrinkage of matter. From a practical standpoint, the temperature linearly decreases from T_0 to T between t=0s and t=5e^{-5}s, and is set to T for t>5e^{-5}s. Besides, the time step is 1e^{-8}s and the total duration is 2.5e^{-4}s which corresponds to a total of 25000 time steps. and no damping is considered. For information purposes, in the sequel, comparisons are also carried out with FEM and DEM based on a discretization of 3200 FE and 15000 particles respectively.

	FEM			*DEM*			*DEM-FEM*		
	A pos.	B pos.	C pos.	A pos.	B pos.	C pos.	A pos.	B pos.	C pos.
u (mm)	6.02e^{-6}	2.02e^{-5}	3.31e^{-5}	5.76e^{-6}	2.03e^{-5}	3.31e^{-5}	5.99e^{-6}	2.01e^{-5}	3.31e^{-5}

Table 2: Displacement values at A, B and C positions at t=5e^{-5}s

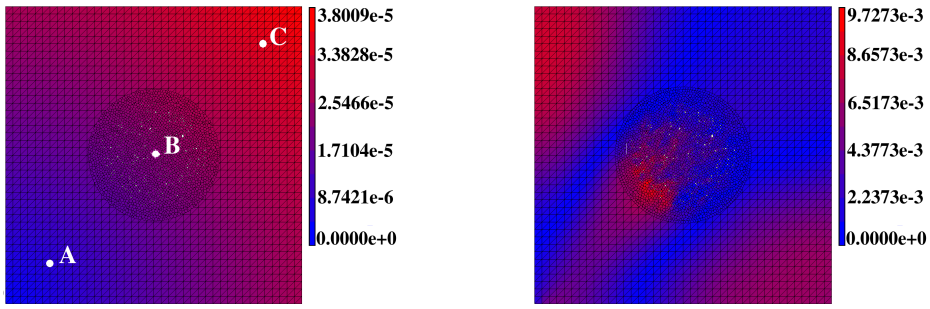

(a) DEM-FEM coupling results

(b) Relative differences between FEM and DEM-FEM coupling

Figure 10: Investigation of the displacement field at t=5e^{-5}s

Figure 10a illustrates the displacement field obtained using the DEM-FEM coupling method at t=5e^{-5}s. From a qualitative standpoint, results verify that the farther away from the origin of coordinates (0;0) we are, higher is the displacement. Quantitatively speaking, comparisons are performed with DEM and FEM using some indicators located at **A** (15mm; 15mm), **B** (50mm; 50mm), and **C** (85mm; 85mm) positions and given in Table 2. Besides, Figure 10b illustrates the relative differences with respect to FE calculations. Numerical comparisons exhibit a quite good agreement between FEM and DEM-FEM coupling with relative differences less than 1% which highlights the suitability of the DEM-FEM coupling in the present context. Figures 11a, b, c and d show some comparative results computed using FEM, DEM and DEM-FEM coupling method in terms of displacement, induced strength, kinetic energy and potential energy. Please keep in mind that what we call ”induced strength” has to be distinguished from the reaction strength. In fact, in DE calculations, if both temperature field and medium are homogeneous, thermal strains do not generate local stress and the material remains relaxed. Conversely, in a FE approach, the thermal expansion is typically

described as an additional force applied to each node of the FE mesh. As a result, the definition of reaction strength is different between both approaches since FE simulations also include a contribution directly related to thermal expansion which does not exist in DEM. That is why, for comparison purposes, we only consider the induced part of the strength as given by DEM, which is theoretically equal to zero in a static case but exhibits some oscillations in a dynamic context. This scope of results exhibits that, whatever the method and the mechanical indicator, results are still in good agreement with relative differences less than 5% with respect to FE references. As a result, we can conclude that DEM-FEM coupling method is able to take into account thermal effects in the present case of a homogeneous material. The next section will focus on heterogeneous materials with thermal-induced damage.

4. Thermal-induced damage in fiber composites

The present section is dedicated to the simulation of fiber composites composed of metallic fibers embedded in an alumina matrix. Investigations are led to exhibit the ability of the DEM-FEM coupling approach to take into account thermal expansion effects and predict the thermal-induced damage at the fiber-matrix interface. In the sequel, all material properties which are given in Table 3 are assumed to be linear elastic.

4.1. Single-fiber composite

4.1.1. Numerical model

In a first step, we consider the case of a single-fiber composite. Numerical simulations are performed using a 2D square pattern of length L=0.1m in which the

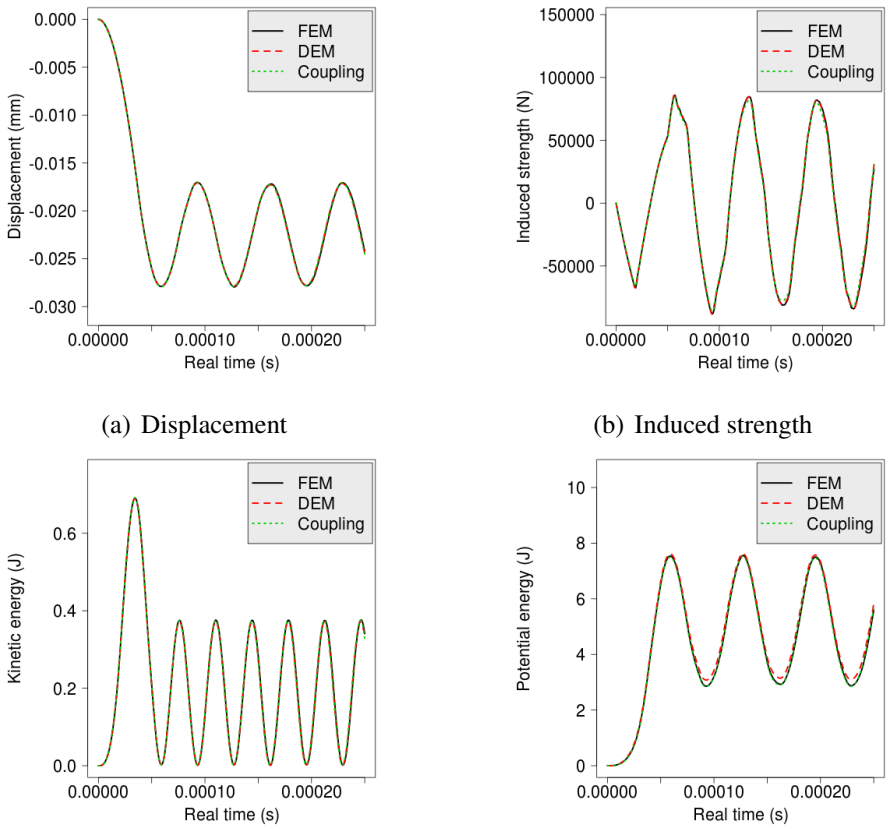

(a) Displacement (b) Induced strength

(c) Kinetic energy (d) Potential energy

Figure 11: Comparison of FEM, DEM and DEM-FEM coupling simulations (case of thermal expansion problem)

single fiber is modeled by a disk of radius R_f=0.015m as described by Figure 12. Thus, the area fraction of the single inclusion with respect to global surface is theoretically 7.07%. Calculations are performed using the DEM-FEM coupling method and compared to FEM. In the coupling approach, we use the same sub-domains as previously seen in the context of a homogeneous material (see Figure 9). The discrete domain is represented by a centered disk of radius R_o=0.023m which encompasses the single-fiber inclusion. The continuous one is delimited by

	Macroscopic properties				*Discrete properties*			
	E_M (Pa)	ν	ρ_M (kg/m^3)	α (/K)	E_μ (Pa)	r_μ	ρ_μ (kg/m^3)	α (/K)
Alumina	350e^9	0.22	3900	7.5e^{-6}	518.5e^9	0.5	4588	7.5e^{-6}
Metal	69.5e^9	0.28	2600	2.25e^{-5}	186.5e^9	0.3	3059	2.25e^{-5}

Table 3: Properties of each phase

the square pattern and an inner circle of radius R_i=0.017m which is higher than R_f so that the continuous part is only constituted of alumina matrix, and l_c=100(R_o-R_i)/L=6%. For information purposes, the granular packing related to DE part is still composed of 2500 particles and the FE one is still discretized using a regular mesh composed of 2892 triangular elements. Please notice that, in DEM-FEM coupling method, the material of each particle is fully determined by the position of its center of mass. Thus, a set of 1073 particles is associated to metallic fiber and a set of 1427 particles is associated to alumina matrix. Preliminary tests exhibit that the representative area of the set of 1073 DE which is calculated by summing the contributions of each particle is 7.06% of the total area and consequently in good agreement with the theoretical area fraction of 7.07%. Conversely to previous studies, a Rayleigh damping is taken into account in our calculations to reduce dynamic effects which could affect the damage process. For simplicity purposes, we only handle a Rayleigh damping matrix proportional to the stiffness matrix in the continuous part and by analogy, proportional to the cohesion matrix given in Equation 3 in the discrete part. The mass proportional Rayleigh damping coefficient is set to 2e^{-6} in both cases. Introducing damping in our calculations directly affects the time step which is now decreased to 2e^{-10}s. However, one has to keep in mind that we consider the same time step for continuous and dis-

crete sub-domains while a multiple time step could have been handled to be more effective.

4.1.2. Elastic response

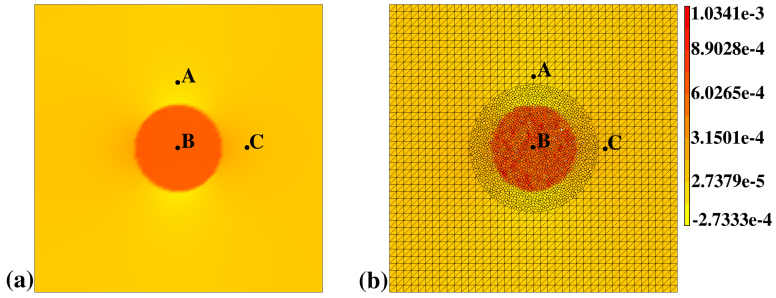

Figure 12: Elastic strain field obtained by (a) FEM and (b) DEM-FEM coupling method (case of single-fiber composite)

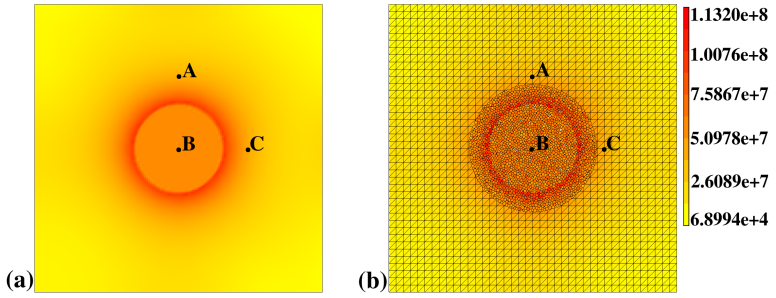

Figure 13: Von-Mises stress field obtained by (a) FEM and (b) DEM-FEM coupling method (case of single-fiber composite)

	FEM (3200 el.)				*FEM (39200 el.)*				*DEM-FEM*			
	A pos.	B pos.	C pos.	max.	A pos.	B pos.	C pos.	max.	A pos.	B pos.	C pos.	max.
ε_e	-9.17e^{-5}	5.36e^{-4}	7.10e^{-5}	6.16e^{-4}	-8.18e^{-5}	5.34e^{-4}	6.30e^{-5}	7.36e^{-4}	-8.81e^{-5}	5.23e^{-4}	6.71e^{-5}	1.03e^{-3}
σ_v	3.08e^{7}	3.91e^{7}	3.08e^{7}	7.45e^{7}	3.42e^{7}	4.12e^{7}	3.42e^{7}	9.64e^{7}	3.21e^{7}	4.06e^{7}	3.30e^{7}	1.13e^{8}

Table 4: ε_e and σ_v (Pa) values at A, B and C positions and corresponding maxima (case of single-fiber composite)

The elastic behavior of the heterogeneous model is investigated using the following configuration. As previously seen in the case of a homogeneous medium, symmetric boundary conditions are imposed at left and bottom edges of the square domain to enable the free expansion of the material. No damage or interfacial effects are taken into account. The temperature field is assumed homogeneous in space but varied over time. In a first phase, the temperature linearly decreases from a given initial value T_0 to a smaller one T with $T=T_0$-50K between t=0s and t=1.6e^{-4}s which corresponds to 800,000 time steps and a gradient of -6.25^{-5}K by time step. In a second phase, the temperature field is maintained constant equal to T for a total duration of 4e^{-4}s which corresponds to a total of 2,000,000 time steps. Figures 12a and b illustrate the elastic strain field respectively given by (a) FEM and (b) DEM-FEM coupling method at t=4e^{-4}s. Please notice that the present FE results are obtained using a mesh composed of 39,200 regular triangular elements which are about 4 times smaller than in the DEM-FEM coupling method to ensure a suitable prediction of stress and strain maxima located close to fiber-matrix interface. Conversely, the coupling method has the great advantage to handle a low density mesh which makes it computationally efficient in comparison with the classical FE method. From a qualitative standpoint, strain fields are very similar with maximum values located in the fiber inclusion. Some quantitative values are extracted from the field at **A**(0.05m;0.075m), **B**(0.05m;0.05m) and **C**(0.075m;0.05m) positions. These indicators and maximum values are given in Table 4 and compared to FE results given by a coarse mesh composed of 3200 elements. At **A**, **B** and **C** positions, the comparison exhibits a good agreement between FEM and DEM-FEM coupling method with relative differences always less than 12% with respect to FE predictions given by the fine mesh. However,

maximum values given by FEM are much lower than those given by the coupling method with relative differences close to 40%. This is explained by disruption effects in the stress field obtained by Zhou's formulation in the discrete sub-domain. In fact, this is only determined at the scale of the particle and could be improved by taking into account the vicinity of each particle using a specific approach. Figures 13a and b show the Von-Mises stress field respectively given by (a) FEM and (b) DEM-FEM coupling method at t=4e^{-4}s. As previously seen in the case of the elastic strain, fields are very similar with maxima located close to the fiber-matrix interface. Quantitative indicators at **A**, **B** and **C** positions highlight suitable results with relative differences less than 10% with respect to FE predictions given by the fine mesh. However, the maximum value is still overestimated by DEM-FEM coupling approach with a relative difference close to 17%. Figures 14a and b illustrate some comparative results computed using DEM and DEM-FEM coupling method in terms of displacement, reaction strength, kinetic energy and potential energy. All results are in very good agreement with relative differences less than 3%. We can conclude that FEM and DEM-FEM coupling method are in good agreement but some local values, especially where strain and stress peaks are noticeable, are somewhat overestimated in the discrete sub-domain.

4.1.3. Thermal-induced damage

We now introduce interfacial debonding effects in our numerical model. Interfacial properties are given by DDZM model discussed in subsection 2.4. Each bond associated to the interface, e.g. each bond connecting two particles belonging to different phases, is modeled by a spring-like element of normal stiffness $\mathrm{K}_n^{\Gamma,0}$ equal to the geometric average of normal stiffnesses K_n^f and K_n^m of beam elements respectively associated to the fiber and the matrix. The interfacial stress limit σ_{lim}^{Γ} is

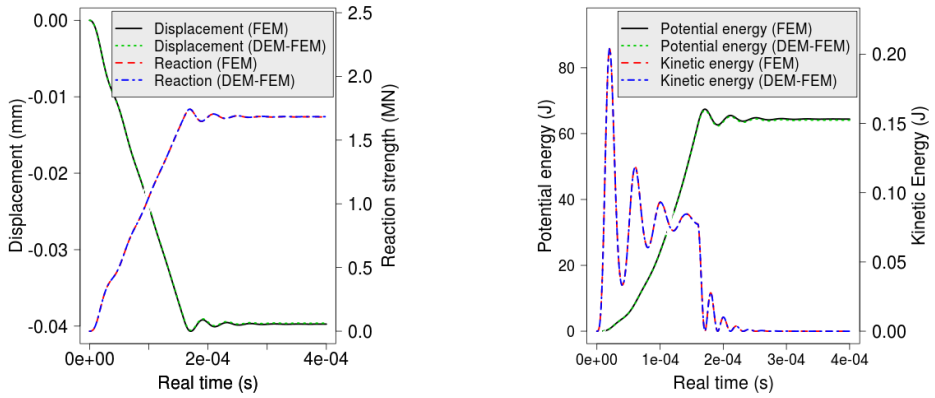

(a) Displacement and reaction field

(b) Kinetic and potential energies

Figure 14: Comparison of FEM and DEM-FEM coupling simulations (case of single-fiber composite)

determined as a function of the stress limit of the matrix σ^m_{lim} using a C_Γ parameter which reads as follows :

$$\sigma^\Gamma_{lim} = C_\Gamma \sigma^m_{lim} \tag{16}$$

In the present study, C_Γ is set to 0.5 which means that the fiber-matrix interface is more prone to break than the matrix when submitted to tensile solicitations. We consider the same mechanical properties and model as previously studied except for the thermal loading. The temperature remains homogeneous in space but is now linearly decreased over time using the same gradient of -6.25^{-5}K by time step until failure without any temperature threshold. Thus, in such a configuration, interfacial debonding theoretically occurs due to the mismatch of CTE between the fiber and the matrix during the cooling process. Figures 15a and b illustrate the Von-Mises stress field around the fiber inclusion when debonding effects initiate at t=1.62^{-4}s and when the fiber-matrix interface is fully debonded at t=2.40^{-4}s. Results exhibit that the debonding occurs shortly after the elastic state discussed

in the previous study, at t=1.62^{-4}s. Local debonding spots appear around the fiber and slowly grows until the fiber-matrix interface is fully debonded at t=2.4^{-4}s. Figure 16 exhibits the evolution of kinetic energy and reaction strength over the time. Please notice that the debonding initiation at t=1.62^{-4}s is materialized by a continuous vertical green line. It is interesting to notice that both parameters are strongly affected by this phenomenon since the kinetic energy tends to zero before damage and a peak occurs at its initiation. Besides, the reaction strength is somewhat disrupted by the debonding. In fact, after breaking and a given period of stabilization, this tends to a linear behavior which signifies that the material is not fully damaged and the matrix is able to respond to the thermal loading in spite of the local damage. These results are in good agreement with our expectations and previous results obtained using full discrete calculations [26]. As a result, we can conclude that DEM-FEM coupling does not disrupt the damage process in the present context.

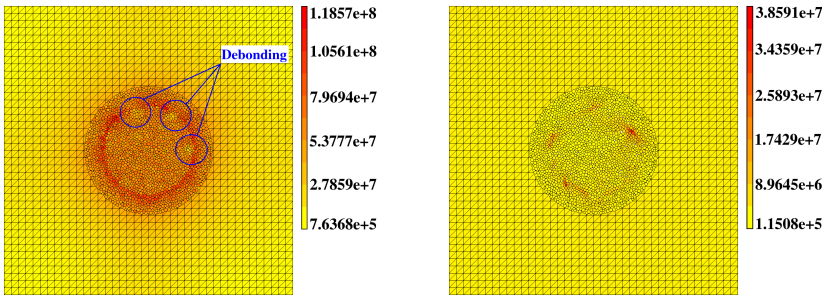

(a) t=1.62^{-4}s, ΔT=-50.6K (b) t=2.40^{-4}s, ΔT=-75.0K

Figure 15: Von-Mises stress field and debonding effects around the fiber inclusion (a) at t=1.6^{-4}s and (b) at t=2.4^{-4}s.

4.2. Multi-fiber composite

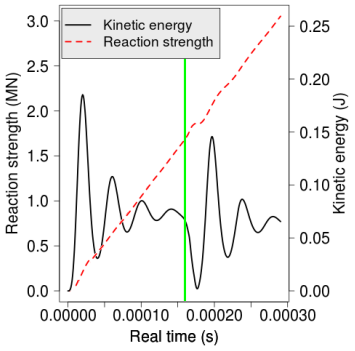

Figure 16: Kinetic energy and reaction strength over the time

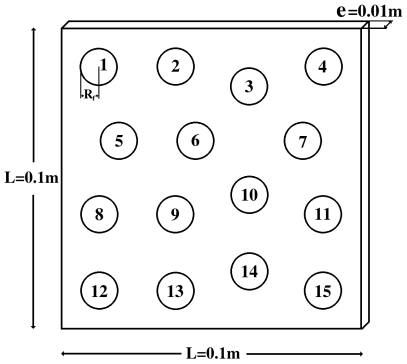

Figure 17: Representative pattern of the multi-fiber composite

4.2.1. Numerical model

We consider the case of a multi-fiber composite modeled by the 2D square pattern of side L=0.1m and thickness e=0.01m described in Fig. 17. The numerical model consists of 15 dilute fibers represented by monodisperse disks of radius R_f=6.35mm so that the total area fraction of fibers is 19.03%. Please notice that the minimum distance between two given inclusions is equal to $2R_f$, and the minimum distance between a given edge and a given disk is R_f. Calculations are carried out using the DEM-FEM coupling method and FEM results are also provided for comparison purposes. Definitions of discrete, continuous and overlapping sub-domains are based on the configuration used in the investigation of the single-fiber composite. A circular discrete area is placed at the center of each inclusion with R_i=1.15R_f and R_o=1.5R_f so that each fiber is fully encompassed in the discrete sub-domain. The continuous sub-domain is delimited by the square pattern and the set of inner circles associated to each inclusion so that this is only composed of alumina matrix. A single granular packing composed of 2500 particles is generated using LSA and replicated to be associated to each discrete area. Thus, the DE

sub-domain is finally composed of a total of 37500 particles. The FE one is discretized using a regular mesh composed of 25220 triangular elements. Moreover, each inclusion is represented by a set of 1073 DE the representation area of which is 1.268% of the total area. Thus, the global ratio for the set of 15 inclusions is 19.02% which is in good agreement with the theoretical value. Identically to the previous study, we use symmetric boundary conditions and a Rayleigh damping is taken into account with a coefficient equal to $6e^{-7}$. Material properties are those given in Table 3 and the time step is set to $1e^{-10}$s.

4.2.2. Elastic response

We aim at investigating the elastic behavior of the multi-fiber composite for a

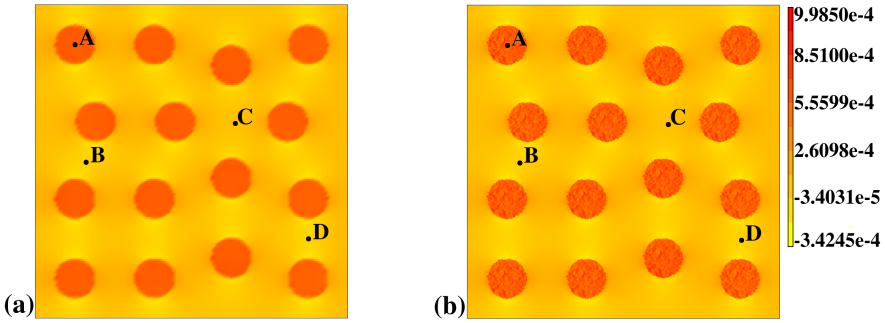

Figure 18: Elastic strain field obtained by (a) FEM and (b) DEM-FEM coupling method (case of multi-fiber composite)

	FEM (64800 el.)					*DEM-FEM*				
	A pos.	B pos.	C pos.	D pos.	max.	A pos.	B pos.	C pos.	D pos.	max.
ε_e	$5.22e^{-4}$	$-1.15e^{-4}$	$-2.61e^{-5}$	$-1.12e^{-4}$	$6.72e^{-4}$	$4.67e^{-4}$	$-1.05e^{-4}$	$-2.53e^{-5}$	$-1.07e^{-4}$	$9.98e^{-4}$
σ_v	$4.82e^{7}$	$4.89e^{7}$	$1.11e^{7}$	$4.46e^{7}$	$1.05e^{8}$	$5.00e^{7}$	$4.70e^{7}$	$1.11e^{7}$	$4.13e^{7}$	$1.36e^{8}$

Table 5: ε_e and σ_v (Pa) values at A, B and C positions and corresponding maxima (case of multi-fiber composite)

given thermal loading. For that purpose, we assume that damage and interfacial

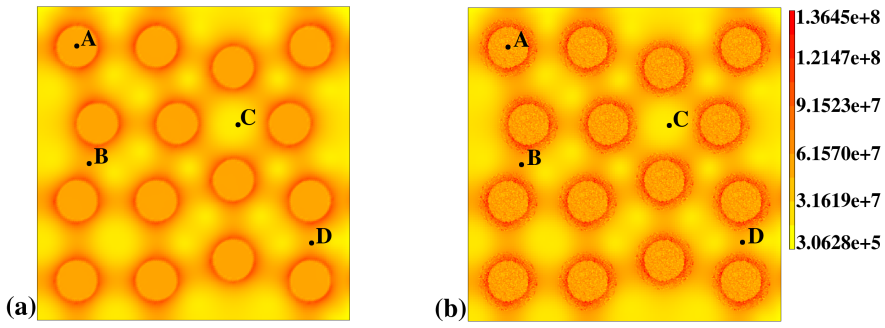

Figure 19: Von-Mises stress field obtained by (a) FEM and (b) DEM-FEM coupling method (case of multi-fiber composite)

debonding do not occur in the present context. The temperature field remains homogeneous in space and time-dependent. Thus, in a first phase, the temperature linearly decreases over time using a gradient of -5.56^{-9}K by time step until a temperature difference of -50K is reached which corresponds to a duration of 9e^{-4}s and a number of 9,000,000 time steps. In a second phase, we consider constant temperature conditions for a total duration of 1.8e^{-3}s which corresponds to a total of 18,000,000 time steps. Figures 18a and b illustrate the elastic strain field obtained at the end of numerical computations at t=1.8e^{-3}s. Results are compared to predictions given by FEM using a regular mesh composed of 64800 triangular elements which is about two times denser than the mesh used in the DEM-FEM coupling method. From a qualitative standpoint, the strain field obtained by the coupling method is very similar to this obtained by the continuous approach. Numerical values are extracted from **A**(12.7mm; 86.8mm), **B**(15.9mm; 49.8mm), **C**(62.7mm; 62.1mm) and **D**(86.8mm; 24.9mm) positions and given in Table 5. The comparison exhibits a good agreement between both approaches with relative differences less than 11% with respect to FE assessments. However, as observed

in the case of the single inclusion problem, maximum values are overestimated in the case of the coupling method. Figures 19a and b illustrate the Von-Mises stress field respectively given by (a) FEM and (b) DEM-FEM coupling method at t=1.8e^{-3}s. Stress fields are very similar and maximum values are located near the fiber-matrix interface as previously observed in the context of a single-fiber composite. Numerical predictions given at **A**, **B**, **C** and **D** positions exhibit the good agreement between both approaches with relative differences less than 8% with respect to FE results. Maximum values are again overestimated. Figures 20a and b provide some comparative results in terms of displacement, reaction strength, kinetic energy and potential energy. All results are in quite good agreement with relative differences less than 5%. In terms of calculation time, numerical computations have been performed using an Intel® Xeon® CPU E5-1660 v2 (3.7 GHz) processor without parallel computing. DEM-FEM coupling based calculations take about 7 days. For comparison, FE calculations based on the mesh of 64800 triangular elements take about 13 days and we estimate that full discrete simulations necessitate more than 3 weeks. To conclude, this scope of results exhibits the relevance of the DEM-FEM coupling method in the present context. However, as regards maximum values, more accurate results could be obtained in the DE part using the vicinity of the particle in the computation of stress and strain fields.

4.2.3. Thermal-induced damage

Interfacial debonding is now taken into account with a C_Γ parameter set to 0.5 so that the fiber-matrix interface is more prone to break than the ceramic matrix. We consider the same mechanical properties as previously used and a spatially homogeneous but time-dependent temperature field is applied using a gradient of -5.56^{-5}K by time step for a total duration of 1.8e^{-3}s. Thus, from a theoretical

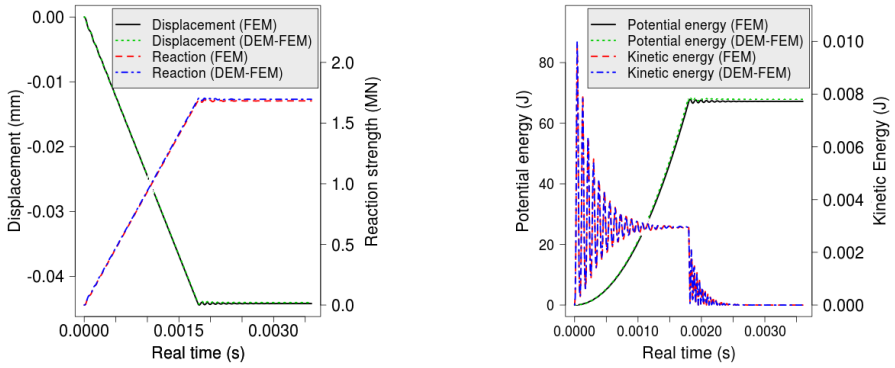

(a) Displacement and reaction field (b) Kinetic and potential energies

Figure 20: Comparison of FEM and DEM-FEM coupling simulations (case of multi-fiber composite)

standpoint, interfacial debonding should occur due to CTE mismatch between the fiber and the matrix during the cooling process. Figures 21a and b show the Von-Mises stress field within the multi-fiber composite when debonding effects initiate at t=7.9^{-4}s and when the fiber-matrix interface is fully debonded at t=8.5^{-4}s. One can notice that the debonding starts at the upper part of the representative pattern at the ceramic-metal interface associated to fibers 1, 3, 4, 5 and 10 with respect to the numbering given in Figure 17. Local debonding spots occur around each fiber and grow until the complete failure of the fiber-matrix interface. This phenomenon propagates to neighboring fibers and a kind of domino effect leads to the complete debonding of the whole set of fibers.

5. Application to a current issue in ceramic-metal joint

5.1. Current issues

Ceramics are widely used in devices in which metal and ceramics have to be jointed together. Thus, among many other applications, ceramic-metal joints ex-

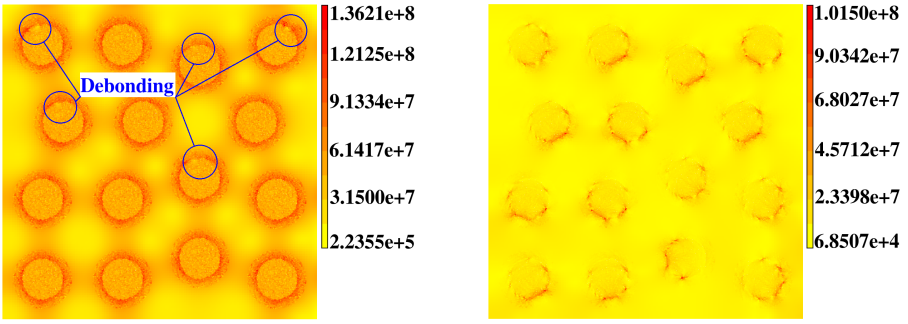

(a) t=7.9^{-4}s, ΔT=-43.8K (b) t=8.5^{-4}s, ΔT=-47.2K

Figure 21: Von-Mises stress field and debonding effects within the multi-fiber composite (a) at t=7.9^{-4}s and (b) at t=8.5^{-4}s.

ist in vacuum tubes, transistor packages and automobile engine components [46]. However, joining ceramic to metal remains a real issue which can be unless partially solved using techniques as the brazing method based on metallic fillers and the solid-state joining. Two main factors affect the quality of joint, namely the CTE mismath and the difference of nature of the interface bond. During a cooling process, CTE mismatch and the difference of mechanical behavior induce thermal stresses which reduce the strength of the material and could lead to unexpected damage of the ceramic-metal joint [47]. As a result, understanding the influence of material properties and other geometrical characteristics on this phenomenon is of crucial importance. In perfect elastic conditions, residual stresses can be estimated knowing mechanical properties and CTE of each material. Typically, residual stresses cause plastic deformations in the metallic part and cracks only arise in the ceramic one. Please notice that the distribution of thermal stresses is not uniformly distributed along the ceramic-metal interface. Thus, residual stresses are more important near the interface and its breadth depends on sample dimensions. Generally speaking the higher the difference of CTE is the lower the strength of

the joint is. However, that is not always true since the presence of internal flaws as voids also induced thermal stresses. Two methods exist to reduce the magnitude of thermal stresses [48]. The first approach consists in inserting a metallic filler with a CTE close to ceramic one. The second approach uses a ductile metal prone to plastic deformations under thermal stresses. Figures 22 illustrate the two main modes of cracking according to the difference of CTE. In the first case depicted in Figure 22a, the CTE of the ceramic α_c is lower than that of the metal α_m. The ceramic part is subjected to tensile solicitations and cracks initiate at the edges near the ceramic-metal interface. In the second case depicted in Figure 22b, the CTE of the ceramic α_c is higher than that of the metal α_m. Tensile stresses are applied at the core of the ceramic part and cracks propagate transversally to the ceramic-metal interface through the ceramic part. Thus, thermal conditions and properties directly impact on the mode of cracking.

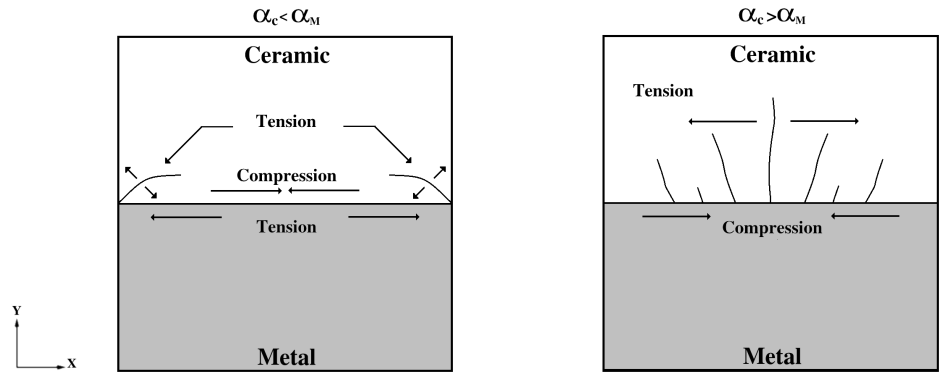

(a) Edge cracks initiation (b) Bulk cracks initiation

Figure 22: Modes of cracking according to the difference of CTE [46, 48]

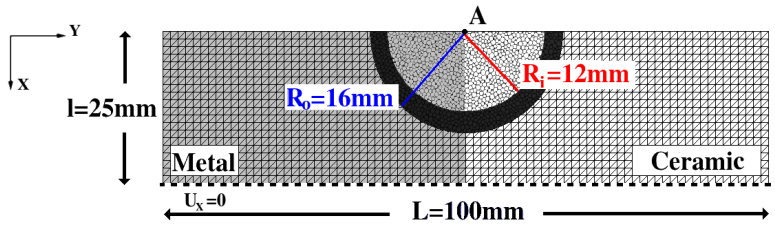

Figure 23: Definition of sub-domains in the DEM-FEM coupling method (case of the ceramic-metal joint problem)

5.2. Numerical simulation

We aim to simulate the case $\alpha_c < \alpha_m$ described in Figure 22a which is more suited to the coupling method due to local damage. The ceramic-metal joint is modeled by a rectangular sample of length L=0.1m and width 2l=0.05m. For efficiency purposes, we only consider one half of the specimen by imposing symmetric boundary conditions at the lower edge of the half-sample. Material properties are given in Table 3 and interfacial debonding and local damage are taken into account. Thus, the ultimate tensile stress of ceramic is set to 200 MPa and C_Γ parameter which describes the interfacial strength is set to 2 so that ceramic is more prone to break than the interface. Figure 23 illustrates the definition of sub-domains in the DEM-FEM coupling method. A half-circular discrete domain of radius R_o=0.0168m and center **A**(0.00m;0.05m) is placed at the upper part of the specimen where local damage should theoretically occur. The continuous one is delimited by the rectangular pattern and a half-circle of same center and radius R_i=0.012m. The granular packing associated to DE part is composed of 4000 particles and the FE Mesh is discretized using 2910 triangular elements. A set of 1952 particles and 276 triangular elements are located within the overlapping area which corresponds to a ratio of one triangular element to about 7 particles.

Calculations are performed using a time step of $3e^{-10}$s and a Rayleigh damping coefficient of $3.6e^{-7}$. The temperature field is assumed homogeneous in space and linearly varied over time using a gradient of -$8.33e^{-6}$K by time step. The total duration of the numerical test is $5.808e^{-3}$s which corresponds to a total of 19,360,000 time steps and a temperature difference ΔT of -161.3K. Figures 24a and b illustrate the Von-Mises stress field before crack initiation at t=$1.82e^{-3}$s, and after failure at t=$3.24e^{-3}$. Figure 24a shows that maximum stress values are located close to ceramic-metal interface with a peak located at the upper left hand corner of the ceramic part. A crack initiates in this area at t=$3.18e^{-3}$s for a temperature difference of -50.7K and propagates to the ceramic core as we can observe in Figure 24b. The crack pattern is in quite good agreement with the expectations depicted in Figure 22a. Figure 25 illustrates the kinetic energy and reaction strength over the time. Results exhibit that the evolution of the kinetic energy is clearly divided in two phases. In a first step, before cracking, the kinetic energy slowly tends to a constant value which is not zero due to linear thermal loading. Then, in a second step, the system is again excited due to crack initiation and propagation and the kinetic energy tends again to the non-zero constant value. The reaction force which is determined by summing the contributions at the lower edge is barely affected by the ceramic cracking. To conclude, DEM-FEM coupling method enables to reproduce a suitable crack pattern in the present context. However, some questions still require some investigations. First, the interfacial parameter C_Γ probably impacts on the numerical output. Then, criteria based on material and geometrical parameters would be useful to determine the suitable size of the overlapping area which has to be optimized to ensure suitable results with a minimum computational cost. Finally, the stress field given by Zhou's formulation at the scale of the

particle is again too disrupted and leads to undesirable local stress peaks which could affect the cracking.

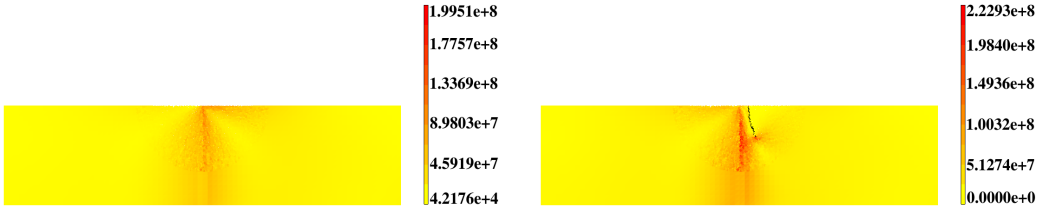

(a) t=1.82^{-3}s, ΔT=-50.7K (b) t=3.24^{-3}s, ΔT=-90.0K

Figure 24: Von-Mises stress field and damage effects (a) at t=1.82^{-3}s and (b) at t=3.24^{-3}s.

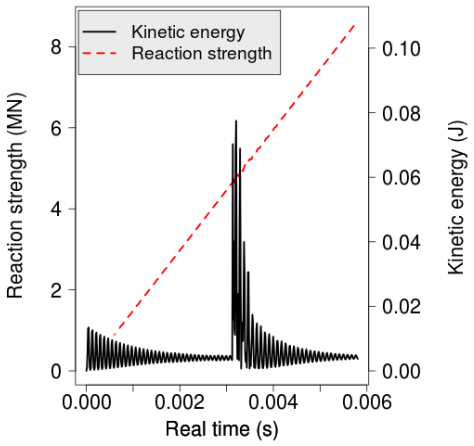

Figure 25: Kinetic energy and reaction strength over the time

Conclusions and prospects

The present work dealt with a DEM-FEM coupling method to simulate the thermal-induced damage in composite materials. In a first step, validation tests performed on a homogeneous medium exhibited the ability of the domain decomposition approach with overlapping area to take into account the thermal expansion. Then,

in a second step, the method was applied to the case of ceramic-metal composites; comparisons with FEM highlighted the accuracy and the efficiency of the discussed method in such a context. Interfacial debonding was also simulated using an interfacial model introduced at the ceramic-metal joint. Results showed suitable debonding effects during a cooling process. Finally, the DEM-FEM coupling method was applied to the framework of ceramic-metal joint issue. Local damage was introduced using a criterion based on the Cauchy stress tensor estimated at the scale of the particle. Numerical simulations led to a proper stress field and a realistic crack pattern. However, stress fields are somewhat disrupted and local peaks could arise at undesirable time and place. We are currently working on a new approach derived from the specimen method proposed by Haddad et al. [18] to solve this issue. In a next future, we expect to set up the present approach in 3D using a parallel implementation of our MULTICOR3D++ code. We are also developing a method to introduce variability effects in the cohesive beam model in the framework of VARIATION project funded by the ”région des Hauts-de-France”.

Conflicts of interest

None declared.

References

[1] Hashin Z. A variational approach to the theory of the elastic behaviour of multiphase materials. J Mech Phys Solids 1963;11(2):127-140.

[2] Mori A, Tanaka K. Average stress in matrix and average elastic energy of materials with misfitting inclusions. Acta Metall 1973;2:571-574.

[3] Torquato S. Random heterogeneous materials. New-York: Springer; 2002.

[4] Moulinec H, Suquet P. A numerical method for computing the overall response of nonlinear composites with complex microstructure. Comput Methods Appl Mech Eng 1998;157:69-94.

[5] Silling S.A. Reformulation of elasticity theory for discontinuities and long-range forces. J Mech Phys Solids 2000;48:175-209.

[6] Cundall PA, Strack ODL. Discrete numerical model for granular assemblies. Geotech 1979;29:47-65.

[7] Fillot N, Iordanoff I, Berthier Y. Modelling third body flows with a discrete element method-a tool for understanding wear with adhesive particles. Tribol Int 2007;40(6):973-981.

[8] Iordanoff I, Elkholy K, Khonsari MM. Effect of particle size dispersion on granular lubrication regimes. Proc Inst Mech Eng J: J Eng Tribol 2008;222(6):725-739.

[9] Nicot F, Hadda N, Guessasma M, Fortin J, Millet O. On the definition of the stress tensor in granular media. Int J Solids Struct 2013;50:2508-2517.

[10] Machado C, Guessasma M, Bellenger E. Electromechanical modeling by DEM for assessing internal ball bearing loading. Mech Mach Theory 2015;92:338-355.

[11] Schlangen E, Garboczi EJ. Fracture simulations of concrete using lattice models : Computational aspects. Eng Fract Mech 1997;57(2):319-332.

[12] Hentz S, Donzé FV, Daudeville L. Discrete element modelling of concrete submitted to dynamic loading at high strain rates. Comput Struct 2004;82(29-30):2509-2524.

[13] Terreros I., Iordanoff I., Charles J.L. Simulation of continuum heat conduction using DEM domains. Comput Mater Sci 2013;69:46-52.

[14] Haddad H, Guessasma M, Fortin J. Heat transfer by conduction using DEM–FEM coupling method. Comput Mater Sci 2014;81:339-347.

[15] Ismail Y, Sheng Y, Yang D, Ye J. Discrete element modelling of unidirectional fibre-reinforced polymers under transverse tension. Compos Part B 2015;73:118-125.

[16] Leclerc W. Discrete Element Method to simulate the elastic behavior of 3D heterogeneous continuous media. Int J Solids Struct 2017;121:86-102.

[17] André D, Iordanoff I, Charles JC, Neauport J. Discrete element method to simulate continuous material by using the cohesive beam model. Comput Methods Appl Mech Eng 2012;213:113-128.

[18] Haddad H, Leclerc W, Guessasma M. Application of DEM to predict the elastic behavior of particulate composite materials. Granul Matter 2015;17:459-473.

[19] Maheo L, Dau F, André, Charles JL, Iordanoff I. A promising way to model cracks in composite using Discrete Element Method. Compos Part B 2015;71:193-202.

[20] Le Bd, Dau F, Charles JL, Iordanoff I. Modeling damages and cracks growth in composite with a 3D discrete element method. Compos Part B 2016;91:615-630.

[21] Leclerc W, Haddad H, Guessasma M. On the suitability of a Discrete Element Method to simulate cracks initiation and propagation in heterogeneous media. Int J Solids Struct 2017;108:98-104.

[22] Jebahi M., Dau F. Iordanoff I., Guin JP. Virial stress based model to simulate the silica glass densification with the discrete element method. Int J Numer Methods Eng 2017;112(13):1909-1925.

[23] Rojek J. Discrete element thermomechanical modelling of rock cutting with valuation of tool wear. Comput Part Mech 2014;1-71-84.

[24] Sinaie S., Heidarpour A., Zhao XL. A micro-mechanical parametric study on the strength degradation of concrete due to temperature exposure using the discrete element. Int J Solids Struct 2016;88-89:165-177.

[25] André D, Levrault B, Tessier-Doyen N, Huger M. A discrete element thermo-mechanical modelling of diffuse damage induced by thermal expansion mismatch of two-phase materials. Comput Methods Appl Mech Eng 2017; 318:898-916.

[26] Leclerc W, Haddad H, Guessasma M. On a discrete element method to simulate thermal-induced damage in 2D composite materials. Comput Struc 2018;196:277-291.

[27] Frangin E, Marin P, Daudeville L. On the use of combined finite/discrete

element method for impacted concrete structures. J Phys 2006; 134:461-466.

[28] Anciaux G, Ramisetti SB, Molinari JF. A finite temperature bridging domain method for MD-FE coupling and application to a contact problem. Comput Methods Appl Mech Eng 2012; 205-208:204-212.

[29] Jebahi M, Charles JC, Dau F, Illoul L, Iordanoff I. 3D coupling approach between discrete and continuum models for dynamic simulations (DEM-CNEM). Comput Methods Appl Mech Eng 2013;255:196-206.

[30] Rousseau J, Frangin E, Marin P, Daudeville L. Multidomain finite and discrete elements method for impact analysis of a concrete structure. Eng Struct 2009;31:2735-2743.

[31] André D, Jebahi M, Iordanoff I, Charles JC, Neauport J. Using the discrete element method to simulate brittle fracture in the indentation of a silica glass with a blunt indenter. Comput Methods Appl Mech Eng 2013;265:136-147.

[32] Liu X, Duddu R, Waisman H. Discrete damage zone model for fracture initiation and propagation. Eng Fract Mech 2012;92:1-18.

[33] Kumar R, Rommel S, Jauffrès D, Lhuissier P, Martin C. Effect of packing characteristics on the discrete element simulation of elasticity and buckling. Int J Mech Sci 2016;110:14-21.

[34] Lubachevsky BD, Stillinger FH. Geometric properties of random disk packings. J Stat Phys 1990;60:561-583.

[35] Donev A, Cisse I, Sachs D, Variano EA, Stillinger FH, Connelly R, et al. Improving the density of jammed disordered packings using ellipsoids. Sci 2004;303:990-993.

[36] Leclerc W, Ferguen N, Pélegris C, Bellenger E, Guessasma M, Haddad H. An efficient numerical model for investigating the effects of anisotropy on the effective thermal conductivity of alumina/Al composites. Adv Eng Softw 2014;77:1-12.

[37] Cambou B. Behaviour of Granular Materials: Micromechanical Approach in Granular Mechanics. 1998.

[38] Zhou M. A new look at the atomic level virial stress : on continuum-molecular system equivalence. Proceedings of the Royal Society of London. Math Phys Eng Sci 2003;2037:2347-2392.

[39] Chang CS, Liao CL. Estimates of elastic modulus for media of randomly packed granules. Appl Mech Rev 1994;47:197-206.

[40] Belytschko T, Xiao S. Coupling methods for continuum model with molecular dynamics. Int J Multiscale Comput Eng 2003;1:115-126.

[41] Xiao S, Belytschko T. A bridging domain method for coupling continua with molecular dynamics. Comput Methods Appl Mech Eng 2004;193(17):1645-1669.

[42] Haddad H, Guessasma M, Fortin J. A DEM-FEM coupling based approach simulating thermomechanical behaviour of frictional bodies with interface layer. Int J Solids Struct 2016;81:203-218.

[43] Tu F, Ling D, Bu L, Yang Q. Generalized bridging domain method for coupling finite elements with discrete elements. Comput Methods Appl Mech Eng 2014;276:509-533.

[44] Chen H, Zang M, Zhang YX. A ghost particle-based coupling approach for the combined finite-discrete element method. Finite Elem Anal Des 2016;114:68-77.

[45] Tu F, Ling D, Hu C, Zhang R. DEM–FEM analysis of soil failure process via the separate edge coupling method. Int J Numer Anal Methods Geomech 2017;41(9):1157-1181.

[46] Uday MB, Ahmad-Fauzi MN, Noor AM, Rajoo S. Current Issues and Problems in the Joining of Ceramic to Metal. Joining technologies 2016.

[47] Palit D, Meier A. Reaction kinetics and mechanical properties in the reactive brazing of copper to aluminum nitride. J Mater Sci 2006;41(21):7197-7209.

[48] Lemus-Ruiz J, Ceja-Cárdenas L, Verduzco J, Flores O. Joining of tungsten carbide to nickel by direct diffusion bonding and using a Cu–Zn alloy. J Mater Sci 2008;43(18):6296-6300.

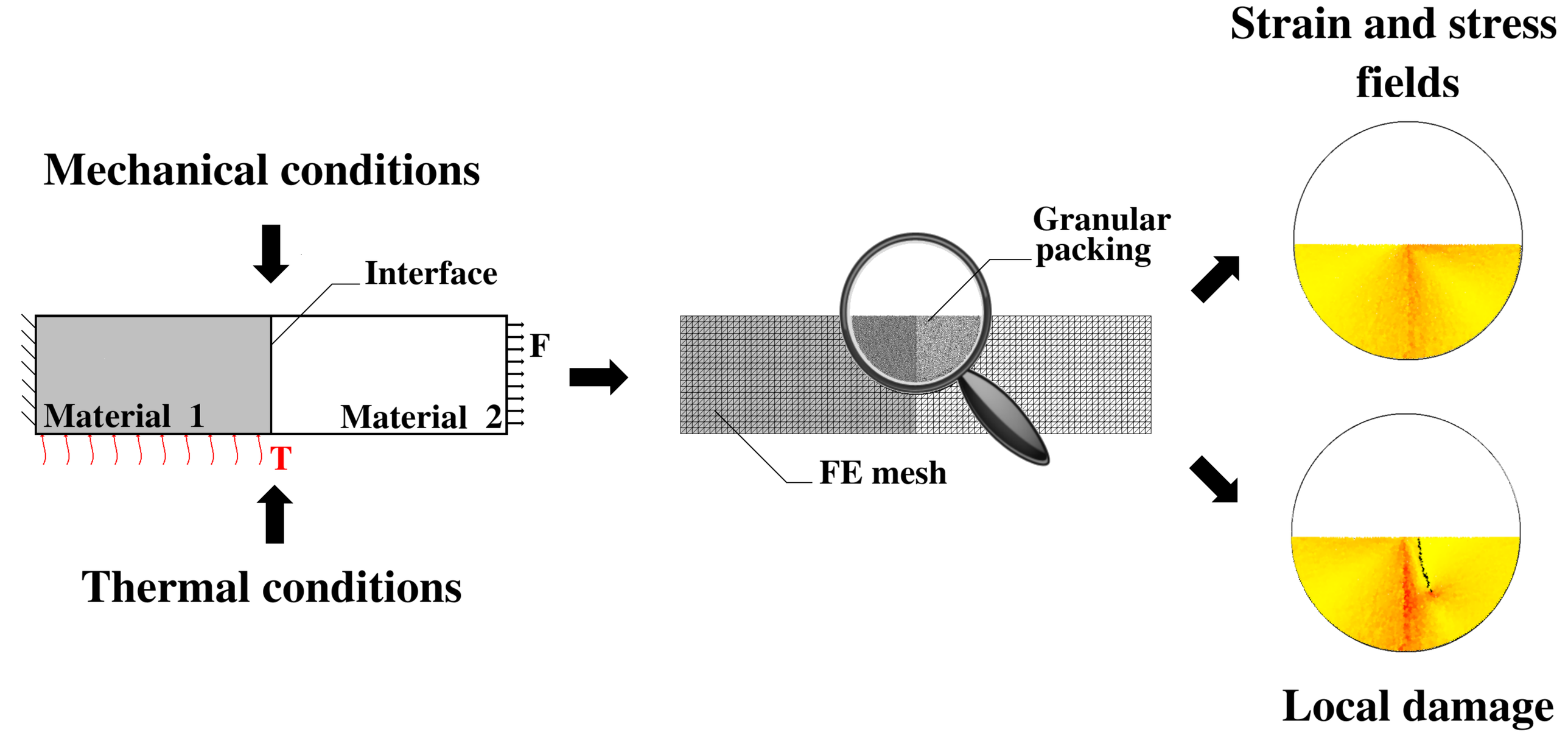
Mechanical conditions
Interface
F
Material 1
Material 2
T
Thermal conditions
Granular packing
FE mesh
Strain and stress fields
Local damage